Published in final edited form as:
Nat Med. 2012 August ; 18(8): . doi:10.1038/nm.2823.

Simultaneous functional photoacoustic and ultrasonic endoscopy of internal organs *in vivo*

Joon-Mo Yang[1], **Christopher Favazza**[1], **Ruimin Chen**[2], **Junjie Yao**[1], **Xin Cai**[1], **Konstantin Maslov**[1], **Qifa Zhou**[2,*], **K. Kirk Shung**[2], and **Lihong V. Wang**[1,*]

[1]Optical Imaging Laboratory, Department of Biomedical Engineering, Washington University in St. Louis, Campus Box 1097, One Brookings Drive, St. Louis, Missouri 63130, USA

[2]National Institutes of Health Ultrasound Transducer Resource Center, Department of Biomedical Engineering, University of Southern California, 1042 Downey Way, University Park, DRB 130, Los Angeles, CA 90089, USA

Abstract

Presently, clinicians routinely apply ultrasound endoscopy in a variety of interventional procedures which provide treatment solutions for diseased organs. Ultrasound endoscopy not only produces high resolution images, it is also safe for clinical use and broadly applicable. However, for soft tissue imaging, its mechanical wave-based image contrast fundamentally limits its ability to provide physiologically-specific functional information. By contrast, photoacoustic endoscopy possesses a unique combination of functional optical contrast and high spatial resolution at clinically-relevant depths, ideal for soft tissue imaging. With these attributes, photoacoustic endoscopy can overcome the current limitations of ultrasound endoscopy. Moreover, the benefits of photoacoustic imaging do not come at the expense of existing ultrasound functions; photoacoustic endoscopy systems are inherently compatible with ultrasound imaging, enabling multi-modality imaging with complementary contrast. Here, we present simultaneous photoacoustic and ultrasonic dual-mode endoscopy and demonstrate its ability to image internal organs *in vivo*, illustrating its potential clinical application.

Endoscopic ultrasound (EUS)[1,2] is currently the most clinically translated tomographic endoscopic imaging modality, and it has made significant contributions to medicine by enabling new interventional procedures in many medical areas, such as gastroenterology[1,3–6], pulmonology[1,7,8], and urology[1,9,10]. Representative applications[1,2] of this technique include EUS-guided sample collection from disease tissue (so-called fine needle aspiration), tissue ablation or endosurgery, interventional device deployment or implantation, and oncologic treatments, such as fine needle injection of chemotherapeutic drugs. Compared to other mainstream medical imaging modalities, such as magnetic resonance imaging, X-ray computed tomography, and positron emission tomography, ultrasound imaging is easily embodied in an endoscopic probe, uses extremely safe

*Correspondence should be addressed to L.V.W (lhwang@biomed.wustl.edu) for the system or to Q.Z. (qifazhou@usc.edu) for the ultrasonic transducers.

AUTHOR CONTRIBUTIONS

J.-M.Y. built the system, performed the experiments, and wrote the manuscript. C.F. developed the data acquisition program, performed the experiments, and co-wrote the manuscript. R.C, Q.Z, and K.K.S. designed and fabricated the ultrasonic transducers. J.Y. contributed to the data processing algorithms and also assisted with data processing and experiments. X.C. helped with the experiments. K.M. contributed to the system development. L.V.W. directed the project, conceived the endoscope design, discussed the experiments, and revised the manuscript.

COMPETING FINANCIAL INTERESTS

L.W. has a financial interest in Microphotoacoustics, Inc. and Endra, Inc., which, however, did not support this work.

mechanical waves, and permits bedside operation. Moreover, it provides high-speed, high-resolution, cross-sectional imaging over a large field-of-view (FOV).

Lung, colorectal, pancreatic, and prostate cancer are leading causes of cancer mortality[11], and all these cancers are located at or close to the respiratory system or gastrointestinal (GI) tract, where endoscopic procedures are applicable. Although EUS-based imaging studies have shown its ability to diagnose these cancers[1,3–10], most of the current applications are primarily focused on guiding other interventional procedures[1,2]. Early stage tumor detection or *in situ* characterization of diseased tissues is challenging for EUS because its contrast mechanism relies on bulk mechanical properties. Tumor boundaries and connections with surrounding blood or lymphatic vessels are clinically relevant and provide necessary information for assessing disease stage or progress[12] and planning treatment therapies. However, pure ultrasound-based image contrast does not sufficiently provide this important information. Recently developed optical endoscopic imaging modalities, such as endoscopic optical coherence tomography[13–15], confocal endoscopy[16], and endoscopic polarized scanning spectroscopy[17,18], can detect diseased tissues and abnormal tissue changes, such as dysplasia, with high sensitivity and high spatial resolution. Still, these techniques are limited by their inability to image targets beyond a ~1–2 mm depth, due to the strong optical scattering of tissue.

Photoacoustic tomography (PAT) is a novel imaging modality that can provide volumetric images of biological tissues *in vivo* with high spatial resolution at super depths[19–21], far exceeding the penetration depths of conventional high-resolution optical imaging modalities[13–18]. PAT systems are very similar to ultrasound imaging systems, because they both employ ultrasound detection to render an image; however, PAT produces images with optical-absorption-based contrast. By utilizing deeply penetrable diffused light to excite photoacoustic signals, PAT can image targets several centimeters deep in soft tissues[21]. With high optical contrast, tumor boundaries and surrounding lymphovascular systems can be resolved with endogenous or exogenous contrast agents[22–26]. Additionally, physiological or functional information, including total hemoglobin concentration, oxygen saturation of hemoglobin (sO_2)[22], blood flow[27], or temperature[28,29], is also measurable. Therefore, photoacoustic endoscopy (PAE)[30] that embodies PAT in a small probe can be used as a new, minimally invasive diagnostic tool which provides optical absorption-based contrast with high spatial resolution, while maintaining the capabilities and benefits of traditional EUS. Here, we report the first *in vivo* demonstrations of simultaneous PAE and EUS imaging in the upper and lower GI tracts of animals with our new integrated endoscopic system.

RESULTS

We developed an integrated PAE and EUS imaging system for simultaneous, photoacoustic (PA) and ultrasonic (US) imaging of internal organs *in vivo* (Fig. 1, Supplementary Figs. 1, 2 and Supplementary Video 1). The US images are produced with conventional pulse-echo imaging that detects acoustic waves reflected from target tissue; the PA images are formed through detection of acoustic waves generated by rapid thermoelastic expansion caused by optical absorption of short laser pulses[21]. A focused US transducer detects one-dimensional depth-resolved signals (or A-lines), and cross-sectional images (or B-scans) are produced by rotating a scanning mirror which directs both optical and acoustic waves. The endoscope system records and displays a set of dual wavelength PA and US B-scan images in real-time during the constant rotation (~4 Hz) of the mirror. By interleaving two optical pulses of different wavelengths and one acoustic pulse at each angular step of the mirror, spatially-coincident images are recorded from the generated PA and US A-line signals, even during periods of significant motion of the target. Volumetric data sets are acquired by recording sequential A-line data during the constant rotational motion of the mirror and mechanical

pullback of the probe at a speed of ~200 μm s^{-1}. Oxy- and deoxy-hemoglobins, two of the dominant absorbers of visible light in most soft biological tissue, have different absorption spectra. With dual-wavelength PA imaging, it is possible to calculate total hemoglobin concentration and sO_2 values (Supplementary Fig. 3)[20,24].

Upper GI tract imaging *in vivo*

We imaged the esophagi of four adult New Zealand white rabbits (Supplementary Fig. 4), and collected 5–10 volumetric data sets from each animal without complications. About 2,800 B-scan slices at ~50 μm intervals were recorded for each volumetric set of PAT at 562 nm, PAT at 584 nm, and US imaging.

The endoscopic system provides anatomic information of the rabbit's esophagus, surrounding tissue, and proximal organs, covering a ~14 cm long, 18 mm diameter volume (Fig. 2 and Supplementary Video 2), within a scanning time of ~12 min. Volume renderings enable three-dimensional (3D) visualization of the morphology and configuration of organs surrounding the esophagus with both contrast mechanisms (Fig. 2a–c, Supplementary Video 3). The PA image (Fig. 2a) was created from data acquired at a 584 nm laser wavelength, in which the PA signal is proportional to the total hemoglobin concentration. Both the PA and US images show the lung and trachea profiles where they abut the esophagus; however, only the PA image provides peripheral vasculature information of these organs. Through trans-esophageal imaging, the tomographic endoscope obtained cross-sectional images of the lung with optical absorption-based contrast (Fig. 2d) and acoustic reflectance-based contrast (Fig. 2e). There were obvious differences in the locations of the contrast origins for the two imaging modes (Fig. 2f). When the endoscope passed by the trachea, strong PA (Fig. 2g) and US (Fig. 2h) signals were observed around the contact point (see the dashed arrow in the two images) between the esophagus and trachea, which run parallel (Fig. 2i) from the cricoid cartilage to the carina. The probe's limited angular FOV covers ~270° only. To obtain a full 360° view, we reinserted the probe with a 180° rotation and imaged the dorsal region of the esophagus. These results are shown in Supplementary Figure 5 and Supplementary Video 4.

For a straightforward comparison of the volumetric images over the entire 360° view, we combined the ventral (Fig. 2) and dorsal (Supplementary Fig. 5) volumetric data sets, using the method described in Supplementary Figure 6, and produced three radial-maximum amplitude projection (RMAP) images, which show the total hemoglobin distribution (Fig. 3a), the sO_2 level (Fig. 3b), and the US echogenicity distribution (Fig. 3c), respectively. To produce the sO_2 distribution over the scanned area (Fig. 3b), dual-wavelength PA data sets were spectrally-analyzed (Supplementary Fig. 3). The 584-nm PA image (Fig. 3a) shows the total hemoglobin distribution in the lung, trachea, and surrounding blood vessels. Also, the aorta and caudal vena cava are shown in the image (Fig. 3a) and are distinguished from each other by differences in sO_2 (Fig. 3b). As confirmed by post-imaging dissection (Supplementary Fig. 7), the heart was located near the mid-ventral line between the two lobes of the lung, and several prominent blood vessels (see the arrow in Fig. 3a), including the aorta and caudal vena cava, branched out from the heart. The aorta and caudal vena cava show reasonable sO_2 values of ~95% and ~70%, respectively (Fig. 3b). The adventitial surface of the trachea and the network of the prominent blood vessels distributed in the apical lung pleura (Fig. 3b) show relatively high sO_2 because they directly receive fully-oxygenated blood from the heart. Strong US contrast was generated at the lung's surface and the trachea (Fig. 3c), which contains cartilage (Fig. 2i). The image reproducibility of the endoscope is presented in Supplementary Figure 8.

Lower GI tract and lymphatic system imaging *in vivo*

We imaged the lower GI tracts of Sprague Dawley rats using the same scanning parameters (Supplementary Fig. 9). Within a scanning time of ~4.6 min, the descending colon of a rat was imaged over a section ~5.5 cm in length and ~12 mm in diameter. Volumetric images clearly show the lumen's architecture (Fig. 4a, Supplementary Video 5). PA imaging shows densely distributed blood vasculature in the colon wall, whereas US imaging shows the density of tissue in the mucosal and submucosal layers, and other mesenteric tissues entangled around the tract. Compared to single-mode EUS[1,6], PAE-EUS provides high-resolution vasculature information in the GI tract and clearly shows optical and mechanical contrast differences. The corresponding sO_2 map (Fig. 4b) reveals the oxygen saturation variation in the imaged blood vessels. The US-RMAP image (Fig. 4c) shows hyperechoic regions generated by the lumen wall and exterior tissues. The PA images also show strong signals from blood vessels; however, corresponding US signals are very weak at those locations (Fig. 4d,e). Although the US imaging provided an approximate boundary profile of the colon, its overall contrast is weak due to the low echogenicity of the soft mucosal tissues (Fig. 4f).

To demonstrate lymphangiographic imaging, we imaged parts of the lymphatic system near the lower GI tracts in Sprague Dawley rats (Supplementary Fig. 10). Accumulation of Evans blue (EB) dye provided the PA image contrast for the lymph nodes and vessels, which are not intrinsically optically absorptive in the visible spectrum. We targeted lymph nodes near the dorsal zone of the descending colon. In these experiments, we utilized 523 nm light to image the surrounding blood vasculature and 640 nm light to image the accumulation of EB in the lymphatic system, which has an absorption peak at ~610 nm (Supplementary Fig. 3). After recording a set of control images, we injected ~0.4-ml EB (0.3%) in the inner legs of the rats, and acquired serial volumetric data sets every 20 minutes for ~1 hour (Supplementary Fig. 11). In each instance, we imaged a volume ~7.2 cm in length and 12 mm in diameter, with a scanning time of ~8 min. Serial PA-RMAP images acquired at 640 nm showed an obvious PA signal increase and dynamic changes of the EB distribution in the lymphatic system, and spectroscopic analysis at the two wavelengths enabled more accurate differentiation between the blood and lymph signals (Supplementary Fig. 11). The strongest EB signals were observed in the PA-RMAP image (Fig. 5c) acquired ~40 min after EB injection, and are clearly different from the control PA-RMAP image (Fig. 5a). However, the corresponding US image (Fig. 5d) did not show any notable changes from the control image (Fig. 5b). Volume rendering of the co-registered dual-wavelength PA and US signals enables 3D visualization of the lymphovascular structure (PAE) inside a density map (EUS) of the tissue (Fig. 5e, Supplementary Videos 6 and 7). As shown in a cross-sectional image (Fig. 5f), the lymph nodes are in contact with the outer colon wall. A spectrally-processed PA-RMAP image (Fig. 5g), which excludes signal from the colon, clearly shows the sO_2 distribution and lymph structures in the imaged anatomy outside the colon and provides a more conducive comparison with the surgical photo (Fig. 5h, Supplementary Fig. 12). Importantly, PAE detected signals from lymph vessels as small as ~1 mm in diameter, far exceeding current capabilities of EUS[1,5,7,8].

DISCUSSION

PAE's unique combination of optical-absorption contrast, wide field-of-view, and large penetration depth suggests many possibilities for medical applications involving diagnostic or interventional procedures. Most of all, it is important to note that PAE can be realized simply through a few modifications and the addition of a light delivery system to EUS technology, while conserving EUS capabilities. The simultaneous, spatially-coincident, PA and US dual-mode imaging provides unprecedented information and promotes morphologic and functional understanding of the target tissue. In the upper GI tract images (Fig. 2),

organs surrounding the esophagus, such as the lung and trachea, were seen in both the PA and US images; however, only PA images showed their adjacent vasculatures. Although contrast-enhanced US techniques[1,9,10], such as Doppler US[1,31], are capable of imaging blood vessels, the technique's sensitivity is much lower than that of PAT, which has recently achieved signal sensitivity high enough to detect single red blood cells[32]. Additionally, PA imaging provides functional information with endogenous contrast (Figs. 2–4), and, with the aid of an exogenous contrast agent, can also provide the dynamics of regional lymph systems (Fig. 5). The experimental results demonstrate the dual-mode endoscope's trans-enteric deep imaging ability and its complementary contrast production.

PAE signal detection is predicated on the same basic principles as EUS signal detection, and the required components for light delivery do not significantly affect the probe's endoscopic functionality. Therefore, this integrated endoscopic technique could be translated into virtually all current application areas of EUS[1,2]. Added angiographic and spectral imaging functions would enhance EUS's role in addressing the aforementioned high-mortality cancers and many other clinical applications. From diagnosis to therapy, possible contributions from PAE are conceived as follows. First, PAE's strong spectroscopic imaging ability and high optical contrast could promote incidental findings of disease symptoms in many routine endoscopic procedures. Tumor detection with conventional single-mode EUS has been a challenge due to the similar mechanical properties of both diseased and healthy soft tissue, and blood and lymph vessels. PAE's spectral imaging ability, based on physiologically-specific endogenous optical contrasts, yields vital functional information, which might enable earlier detection of tissue abnormalities. Additionally, based on the lymphovascular information that PAE can provide, it might improve the accuracy of cancer staging. Contrast agents for EUS are limited, while PAE's unique broad-spectrum, absorption-based contrast fosters the use of various kinds of contrast agents[24–26], enabling many applications, such as lymph node mapping[23,26] and molecular imaging for cancer mapping and staging[12,24,25,33]. Lastly, PAE's high contrast and high resolution vasculature imaging ability could enable more advanced interventional procedures by helping practitioners guide devices to extract samples for biopsy or to inject drugs for chemotherapy.

Another key feature of PAT is its exceptional scalability[21], spanning from sub-cellular resolution at shallow depths to providing optical contrast of tissue more than several centimeters deep with ultrasound-level spatial resolution. For lumen wall imaging in which large penetration depth is not necessary, optically-resolved PA imaging could provide greater spatial resolution[32]. In many clinical trans-enteric imaging applications, deep imaging ability is more important. Choosing a lower center frequency transducer, red-shifting laser wavelengths to the near-infrared spectrum, or increasing the laser pulse energy by enlarging the illumination area all would greatly improve the penetration depth of PAE, making it more applicable to current clinical requirements (more technical discussion is available in the Supplementary Discussion). In this study, we employed a pair of laser beams at 584 nm and 562 nm to determine distributions of total hemoglobin concentration and sO_2, and another pair at 640 nm and 523 nm to image the lymphovascular system with the aid of a contrast agent. However, one can freely choose illumination wavelengths, from ultraviolet to near-infrared, to quantitatively evaluate other cellular or physiological constituents, such as cell nuclei[34] or hydration levels[35]. Further, more laser pulses can be added to each angular step of the mirror to generate richer spectral information for more thorough characterization of diseased tissues. With the integration of PAE, EUS could become a more powerful clinical tool.

ONLINE METHODS

Integrated PA and US endoscopic probe

We designed and implemented a new endoscopic probe for simultaneous PA and US imaging. The new probe has a streamlined shape and is smaller (outer diameter 3.8 mm, 38 mm rigid distal length) than our first generation probe[30]. To improve the overall image quality, transverse resolution, and the signal sensitivity, we fabricated a focused US transducer with a piezo-element of single crystal $LiNbO_3$ (~36 MHz, 65% fractional bandwidth), with a 2.6-mm aperture and a 0.5-mm diameter central hole to route the optical fiber that delivers laser beams. To equip the probe with the capability of rotational scanning, we incorporated a built-in actuator (Fig. 1a) comprised of a micromotor (Namiki Precision Inc.) and other mechanical components necessary for water sealing (Supplementary Fig. 1). We encapsulated the optical fiber, the transducer's signal wires, and the actuator's electric wires in a ~1 m long, flexible plastic sheath.

Dual-wavelength PA and US endoscopic imaging system

For dual-wavelength PA imaging, we employed two identical pulsed laser systems to generate the first and second laser wavelengths. Each system was comprised of a tunable dye laser (Cobra HRR, Sirah) pumped by a solid-state, diode-pumped Nd:YLF laser (INNOSLAB IS811-E, EdgeWave). We utilized an ultrasonic pulser-receiver (5072 PR, Panametrics-NDT, Olympus), which provided sharp electric pulses to the US transducer to generate acoustic pulses for US imaging and also amplified the US and PA signals detected by the transducer. More detailed information on the connection of these systems is provided in Supplementary Figure 1.

Data acquisition and processing

We developed a LabVIEW (National Instruments) software-based data acquisition program which records and displays dual-wavelength PA and US B-scan images in real time (~4 Hz) during the endoscopic imaging procedure. We produced the volumetric images after performing each animal experiment. In the US B-scan images, strong acoustic reflections were generated by the plastic membrane (imaging window) of the probe. The reflected signals identified the boundary of the membrane. We filtered out the multiple reverberation signals generated by the membrane throughout the entire US B-scan image. We applied envelope detection to all PA and US A-line data, and time-gain compensation to the extracted amplitude signals. To produce volumetric images of the upper GI tract, we employed a surface alignment algorithm and simple spatial filtering, at the expense of image resolution, to reduce the strong motion artifacts primarily caused by periodic respiration.

Upper GI tract imaging of rabbits

We imaged the esophagi of adult New Zealand white rabbits (~4 kg, Myrtles Rabbitry). The rabbits were fasted, beginning ~12 hr before the experiments, to reduce the likelihood of ingesta in the stomach and esophagus. We anesthetized the rabbits with 35–50 mg kg^{-1} of ketamine and 5–10 mg kg^{-1} of xylazine (IM). While anesthetized, the rabbit was intubated and supplied with maintenance gas for anesthesia (1.5–3.0% isoflurane). We inserted an endotracheal tube cuff into the trachea and inflated it to prevent aspiration of water into the lung. We placed the rabbit on an inclined stage (~10°) in supine position. Just prior to probe insertion, we introduced water into the esophagus and stomach, using an enteral feeding syringe connected to a rubber feeding tube (8–12 F). The water provided the necessary acoustic coupling and functioned as a lubricant during the imaging procedure. After filling the stomach and esophagus with water, we inserted the endoscopic probe through the mouth and advanced ~30 cm into the esophagus, and immediately initiated endoscopic imaging.

Throughout the experiment, we continuously monitored the rabbit's anesthesia level and vital signs. After the experiment, we euthanized the rabbit by an overdose of pentobarbital (150 mg kg^{-1}) injected in the marginal ear vein.

Lower GI tract imaging of rats

We imaged the colons of adult Sprague Dawley rats (~450 g; Harlan National Customer Service Center). The rats were fasted for ~12 hr before the experiments, to increase the likelihood of an empty colon for imaging. In each experiment, we anesthetized the rat with 4% isoflurane for induction, and administered a cocktail of 87 mg kg^{-1} ketamine and 13 mg kg^{-1} xylazine (IP) to provide time to prepare and mount the animal. After properly positioning the animal, we inserted medical ultrasound gel into the descending colon via a small plastic tube. The ultrasound gel provided acoustic coupling between the tissue and ultrasound transducer and lubricated the probe during colon insertion through the anus. While imaging, we maintained anesthesia with 1.5–2.0% isoflurane supplied through a nose cone. After the experiment, we euthanized the rat by a pentobarbital overdose (150 mg kg^{-1}, IP).

All procedures in the animal experiments followed the protocol approved by the Institutional Animal Care and Use Committee at Washington University in St. Louis. To validate the imaging results, we excised tissue samples and histologically analyzed after standard H&E staining.

Supplementary Material

Refer to Web version on PubMed Central for supplementary material.

Acknowledgments

We thank J. Ballard for his attentive reading of the manuscript. We also thank J. Kalishman, P. Jiménez-Bluhm, and L. Andrews-Kaminsky for helping with the animal preparation, surgery, and image interpretation. We thank B. Matthews, V. Tsytsarev, G. Lanza, R. Senior, and J. Atkinson for helpful discussion on the experimental results. This work was sponsored in part by US National Institutes of Health grants R01 CA157277, R01 NS46214 (BRP), R01 EB000712, R01 EB008085, P41-EB2182, and U54 CA136398 (Network for Translational Research). J.-M.Y. was supported in part by a Korea Research Foundation Grant funded by the Korean Government (KRF-2007-357-C00039).

REFERENCES

1. Dietrich, C., editor. Endoscopic Ultrasound: An Introductory Manual and Atlas. New York: Thieme; 2006.
2. Kaul V, et al. Interventional EUS. Gastrointest Endosc. 2010; 72:1–4. [PubMed: 20381044]
3. Rosch T, et al. Localization of pancreatic endocrine tumors by endoscopic ultrasonography. N Engl J Med. 1992; 326:1721–1726. [PubMed: 1317506]
4. Gress FG, Hawes RH, Savides TJ, Ikenberry SO, Lehman GA. Endoscopic ultrasound-guided fine-needle aspiration biopsy using linear array and radial scanning endosonography. Gastrointest Endosc. 1997; 45:243–250. [PubMed: 9087830]
5. Chang KJ, Nguyen P, Erickson RA, Durbin TE, Katz KD. The clinical utility of endoscopic ultrasound-guided fine-needle aspiration in the diagnosis and staging of pancreatic carcinoma. Gastrointest Endosc. 1997; 45:387–393. [PubMed: 9165320]
6. Fu KI, et al. Staging of early colorectal cancers: magnifying colonoscopy versus endoscopic ultrasonography for estimation of depth of invasion. Dig Dis Sci. 2008; 53:1886–1892. [PubMed: 18080834]
7. Silvestri GA, et al. Endoscopic ultrasound with fine-needle aspiration in the diagnosis and staging of lung cancer. Ann Thorac Surg. 1996; 61:1441–1445. discussion 1445–1446. [PubMed: 8633956]

8. Navani N, Spiro SG, Janes SM. Mediastinal staging of NSCLC with endoscopic and endobronchial ultrasound. Nat Rev Clin Oncol. 2009; 6:278–286. [PubMed: 19390554]
9. Salomon G, et al. Evaluation of prostate cancer detection with ultrasound real-time elastography: a comparison with step section pathological analysis after radical prostatectomy. Eur Urol. 2008; 54:1354–1362. [PubMed: 18374470]
10. Trabulsi EJ, Sackett D, Gomella LG, Halpern EJ. Enhanced transrectal ultrasound modalities in the diagnosis of prostate cancer. Urology. 2010; 76:1025–1033. [PubMed: 20719368]
11. Jemal A, Siegel R, Xu J, Ward E. Cancer statistics, 2010. CA Cancer J Clin. 2010; 60:277–300. [PubMed: 20610543]
12. Steeg PS. Tumor metastasis: mechanistic insights and clinical challenges. Nat Med. 2006; 12:895–904. [PubMed: 16892035]
13. Tearney GJ, et al. In vivo endoscopic optical biopsy with optical coherence tomography. Science. 1997; 276:2037–2039. [PubMed: 9197265]
14. Yun SH, et al. Comprehensive volumetric optical microscopy in vivo. Nat Med. 2006; 12:1429–1433. [PubMed: 17115049]
15. Adler DC, et al. Three-dimensional endomicroscopy using optical coherence tomography. Nat Photon. 2007; 1:709–716.
16. Kiesslich R, et al. Confocal laser endoscopy for diagnosing intraepithelial neoplasias and colorectal cancer in vivo. Gastroenterology. 2004; 127:706–713. [PubMed: 15362025]
17. Qiu L, et al. Multispectral scanning during endoscopy guides biopsy of dysplasia in Barrett's esophagus. Nat Med. 2010; 16:603–606. 601p following 606. [PubMed: 20383155]
18. Terry NG, et al. Detection of dysplasia in Barrett's esophagus with in vivo depth-resolved nuclear morphology measurements. Gastroenterology. 2011; 140:42–50. [PubMed: 20854820]
19. Oraevsky, AA.; Karabutov, AA. Optoacoustic Tomography. In: Vo-Dinh, T., editor. Biomedical Photonics Handbook. Vol. Vol. PM125. New York: CRC Press; 2003. p. 3401-3434.
20. Wang, LV., editor. Photoacoustic Imaging and Spectroscopy. Boca Raton: CRC; 2009.
21. Wang LV. Multiscale photoacoustic microscopy and computed tomography. Nat Photonics. 2009; 3:503–509. [PubMed: 20161535]
22. Zhang HF, Maslov K, Stoica G, Wang LV. Functional photoacoustic microscopy for high-resolution and noninvasive in vivo imaging. Nat Biotechnol. 2006; 24:848–851. [PubMed: 16823374]
23. Erpelding TN, et al. Sentinel lymph nodes in the rat: noninvasive photoacoustic and US imaging with a clinical US system. Radiology. 2010; 256:102–110. [PubMed: 20574088]
24. Kim C, Favazza C, Wang LV. In vivo photoacoustic tomography of chemicals: high-resolution functional and molecular optical imaging at new depths. Chem Rev. 2010; 110:2756–2782. [PubMed: 20210338]
25. De La Zerda A, et al. Carbon nanotubes as photoacoustic molecular imaging agents in living mice. Nat Nano. 2008; 3:557–562.
26. Kim J-W, Galanzha EI, Shashkov EV, Moon H-M, Zharov VP. Golden carbon nanotubes as multimodal photoacoustic and photothermal high-contrast molecular agents. Nat Nano. 2009; 4:688–694.
27. Yao J, Maslov KI, Shi Y, Taber LA, Wang LV. In vivo photoacoustic imaging of transverse blood flow by using Doppler broadening of bandwidth. Opt Lett. 2010; 35:1419–1421. [PubMed: 20436589]
28. Irina VL, et al. Real-time optoacoustic monitoring of temperature in tissues. Journal of Physics D: Applied Physics. 2005; 38:2633.
29. Shah J, et al. Photoacoustic imaging and temperature measurement for photothermal cancer therapy. J Biomed Opt. 2008; 13 034024.
30. Yang JM, et al. Photoacoustic endoscopy. Opt Lett. 2009; 34:1591–1593. [PubMed: 19448831]
31. Xuan JW, et al. Functional neoangiogenesis imaging of genetically engineered mouse prostate cancer using three-dimensional power Doppler ultrasound. Cancer Res. 2007; 67:2830–2839. [PubMed: 17363606]

32. Zhang C, Maslov K, Wang LV. Subwavelength-resolution label-free photoacoustic microscopy of optical absorption in vivo. Opt Lett. 2010; 35:3195–3197. [PubMed: 20890331]

33. Weissleder R, Pittet MJ. Imaging in the era of molecular oncology. Nature. 2008; 452:580–589. [PubMed: 18385732]

34. Yao DK, Maslov K, Shung KK, Zhou Q, Wang LV. In vivo label-free photoacoustic microscopy of cell nuclei by excitation of DNA and RNA. Opt Lett. 2010; 35:4139–4141. [PubMed: 21165116]

35. Xu Z, Li C, Wang LV. Photoacoustic tomography of water in phantoms and tissue. J Biomed Opt. 2010; 15 036019.

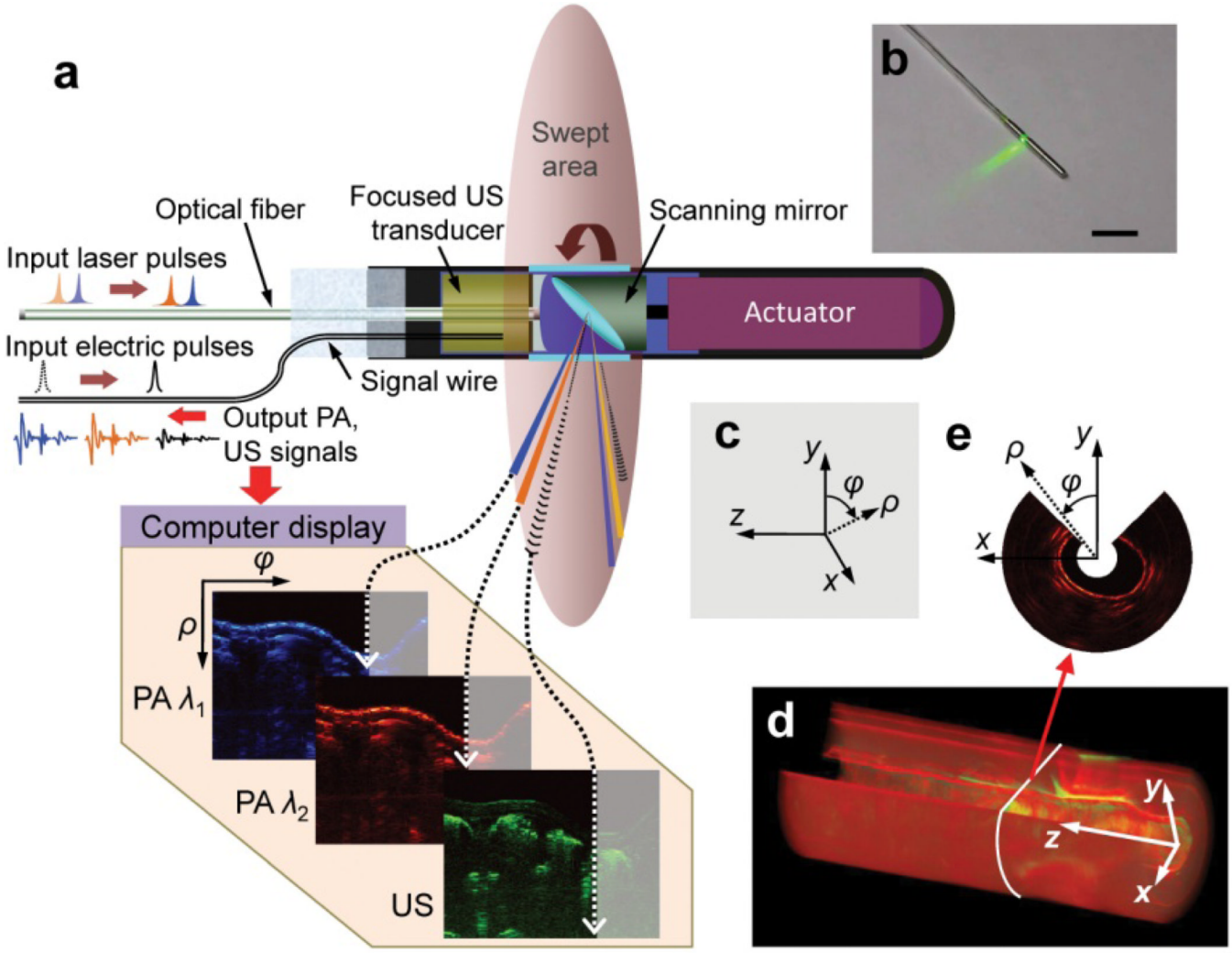

Figure 1.

Illustration of simultaneous, multi-wavelength photoacoustic (PA) and ultrasonic (US) endoscopy. (**a**) The endoscope performs circumferential sector scanning by rotating a scanning mirror, which reflects both the US waves and laser pulses and enables static mounting of the associated illumination and US pulse generation-detection units. At each angular step of the mirror (~1.42°), both the first (λ_1) and second (λ_2) pulsed laser beams are independently fired through the optical fiber and the acoustic pulse is generated by the US transducer with a constant time delay of ~30 μs between each of the laser and acoustic pulses. The ensuing PA and US echo waves are detected and converted into electric signals by the US transducer; the signals are then recorded and displayed on a computer. The 30-μs time delay is necessary to ensure that the sample has relaxed and that consecutive signals will not interfere with each other. However, this delay does not significantly affect co-registration of the three images because the difference between the angular positions of each signal is small and is well within the spatial resolution of the detector. (**b**) A photo shows the side-scanning 3.8-mm diameter probe prototype firing a 562 nm laser beam. Scale bar, 2 cm. (**c**) Definition of Cartesian and cylindrical coordinate systems. The +*z*-axis is defined along the endoscope axis (or pullback direction). (**d**) A volumetric image comprised of consecutive B-scan slices. (**e**) A representative cross-section of **d** along the *x*-*y* plane, which shows the endoscope's 270° angular FOV.

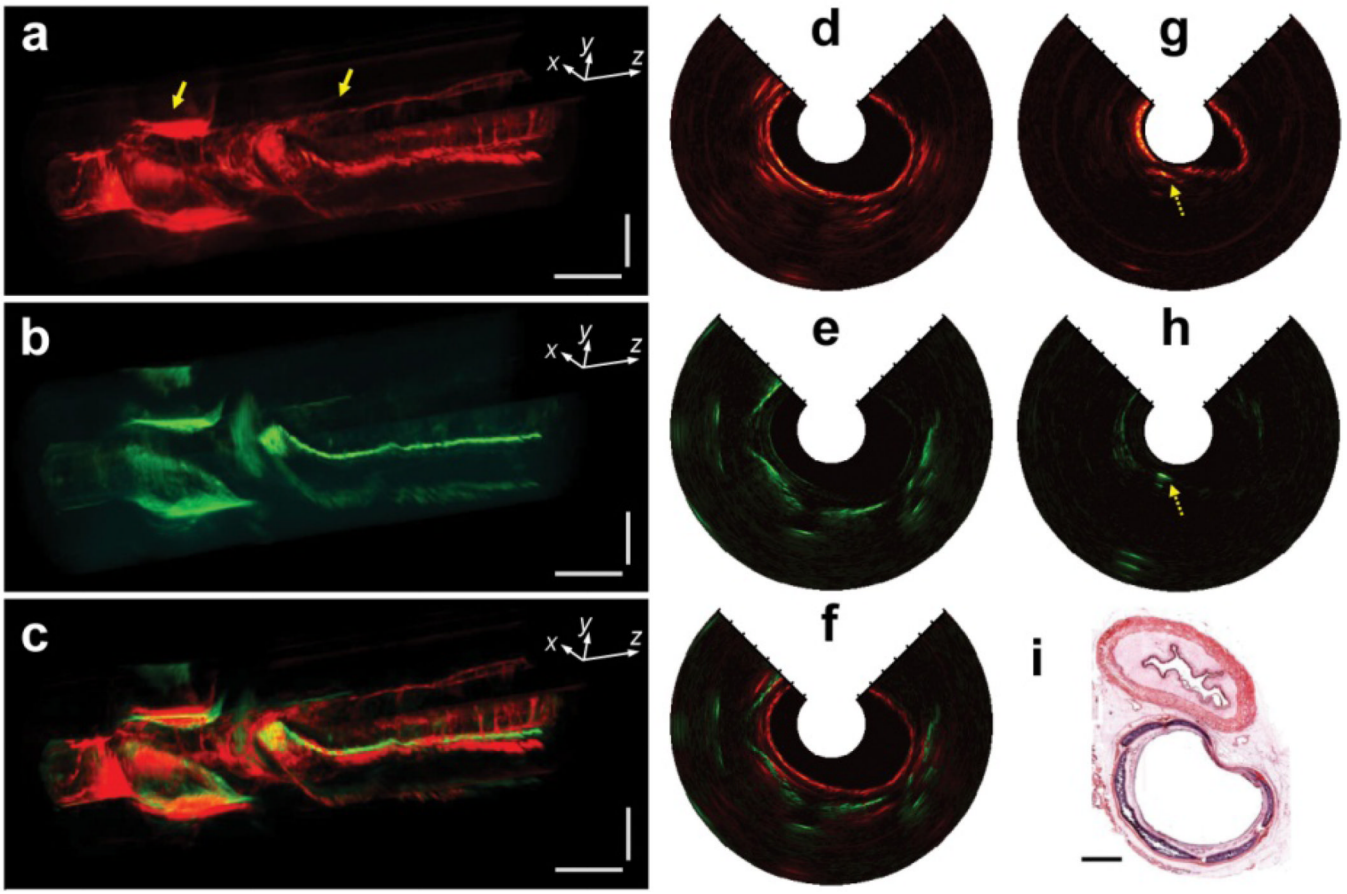

Figure 2.

Simultaneous, co-registered, PAE-EUS pseudo-color images from a rabbit esophagus *in vivo*. (**a**) Three-dimensionally rendered PA structural image. The left-and right-hand sides of this image correspond to the lower and upper esophagus, respectively, and the lower portion (–*y* axis) to the ventral side of the animal. To more clearly display the structures surrounding the esophagus, we excluded signals generated from the esophagus. (**b**) Co-registered US structural image for the same volume of **a**. (**c**) An overlaid image of **a** and **b**. In **a–c**, the horizontal and vertical scale bars represent 2 cm and 5 mm, respectively. (**d**) A representative PA *x*-*y* cross-sectional image (18 mm diameter) near the lung, as indicated by the left arrow in **a**. The ~0.8 mm thick region from the inner surface of the imaged lumen represents the signals from the esophagus. The surface of the lung is shown ~1 mm from the inner surface. (**e**) Corresponding US cross-sectional image of **d**. (**f**) A combined image of **d** and **e**. (**g**) A representative PA *x*-*y* cross-sectional image (18 mm diameter) near the trachea, as indicated by the right arrow in **a**. (**h**) Corresponding US cross-sectional image of **g**. In **d–h**, the hash marks represent 1 mm intervals. (**i**) Representative histology (H&E stain) of the esophagus (upper) and trachea (lower). Scale bar, 1 mm.

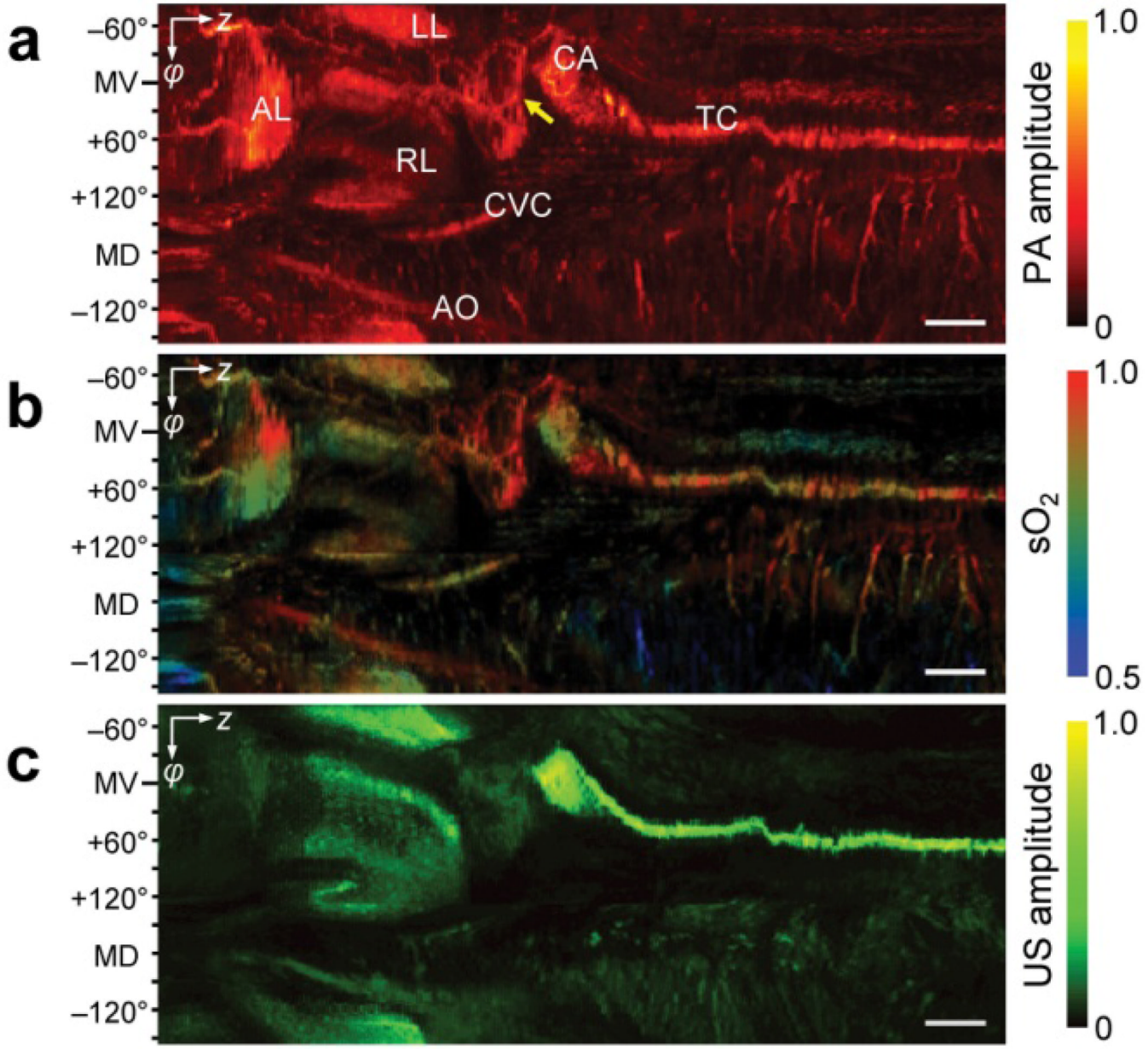

Figure 3.

Radial-maximum amplitude projection (RMAP) images over a full 360° angular FOV (views from the inside of the esophagus). The left-and right-hand sides of these three images correspond to the lower and upper esophagus, respectively. (**a**) Normalized PA-RMAP image showing the total hemoglobin distribution, with the esophageal signals excluded during the RMAP construction. AL, accessory lobe; LL, left lobe; RL, right lobe of the lung; AO, aorta; CVC, caudal vena cava; CA, carina; TC, trachea. (**b**) Functional PA-RMAP image showing the sO_2 levels of the imaged structures in **a**. (**c**) Normalized US-RMAP image showing the echogenicity distribution. In each image, the vertical ϕ-axis corresponds to the angular range of 360°, and the horizontal *z*-axis corresponds to the pullback length of 14 cm. The approximate mid-ventral (MV) position and angular measures from the MV are marked along the vertical ϕ-axis, where the positive and negative values correspond to the

right and left sides of the animal, and MD denotes the mid-dorsal position. The scale bars represent 1 cm for the horizontal direction only.

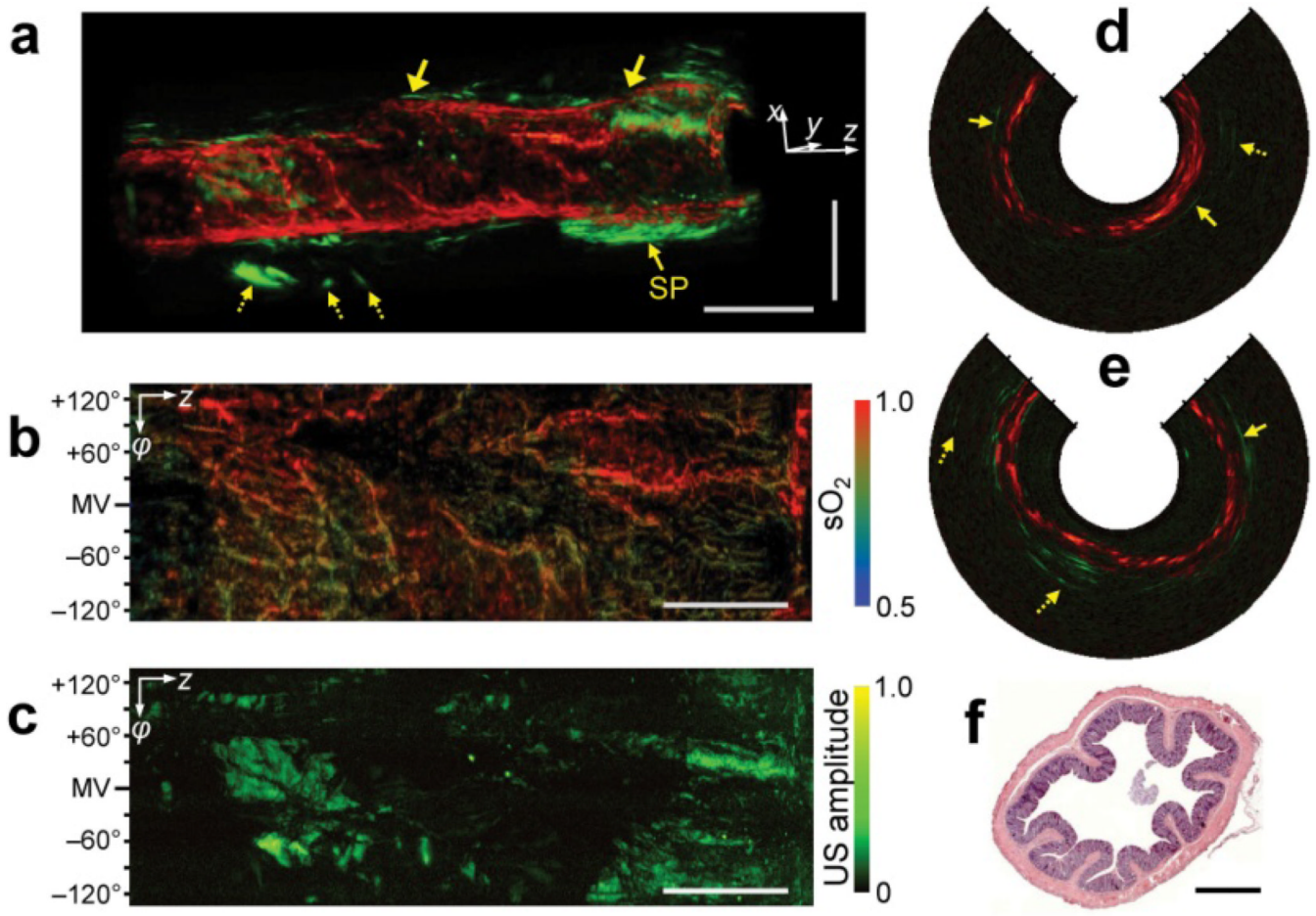

Figure 4.

Simultaneous, co-registered, PAE-EUS colonoscopic pseudo-color images of a rat colon acquired *in vivo*. (**a**) Three-dimensionally rendered PA-US structural image. The right side of this image is closer to anus, and the negative *y*-axis corresponds to the ventral direction of the animal. The red and green colors correspond to PA and US signals, respectively. The dashed arrow indicates mesenteric tissue entangled around the tract, and SP denotes the sphincter. The horizontal and vertical scale bars represent 1 cm and 5 mm, respectively. (**b**) PA-RMAP image showing the sO_2 levels of the imaged structures in **a** (views from the inside of the colon). (**c**) Corresponding US-RMAP image showing the echogenicity distribution. In **b** and **c**, the vertical ϕ-axis corresponds to the angular FOV covering 270°, and the horizontal *z*-axis corresponds to the pullback length of 5.5 cm. The approximate mid-ventral (MV) position and angular measures from the MV are marked along the vertical ϕ-axis, where the positive and negative values correspond to the right and left sides of the animal. The scale bars represent 1 cm for the horizontal direction only. (**d,e**) PA-US cross-sectional images from the position indicated by the left and right arrows in **a**, respectively. In **d** and **e**, the solid arrows indicate the outer boundary of the colon, and mesenteric tissues are marked with dashed arrows. The hash marks represent 1 mm intervals. (**f**) A typical histology image (H&E stain) of the colon. Scale bar, 1 mm.

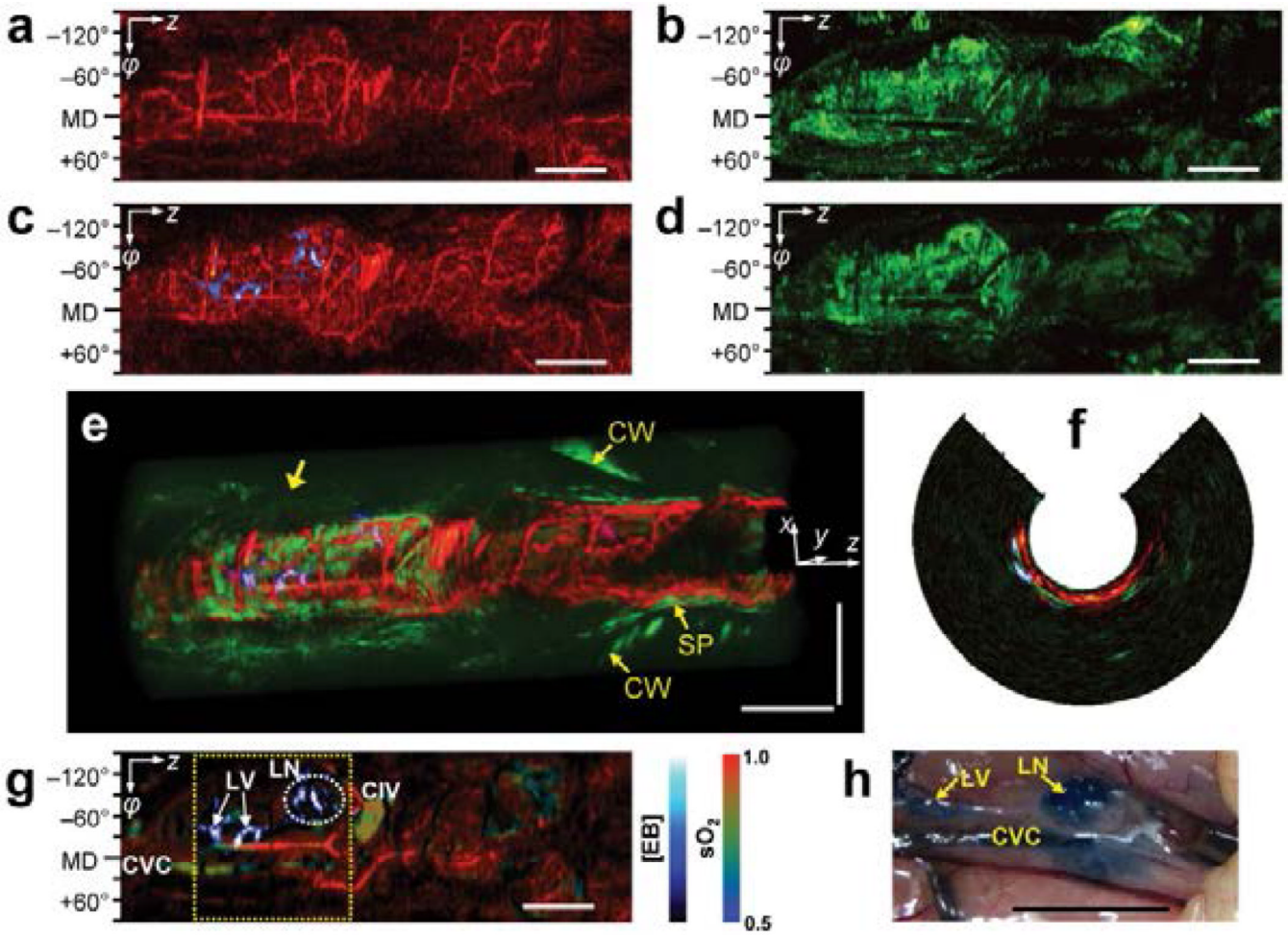

Figure 5.

Lymphovascular system imaging *in vivo* near a rat colon. (**a**) Control PA-RMAP image before EB administration (views from the inside of the colon). The right side of this image is closer to the anus. (**b**) Co-registered US-RMAP image of **a**. (**c**) PA-RMAP image at ~40 min post-injection (processed from the dual-wavelength data). The red and blue colors represent PA signals from blood and EB, respectively. (**d**) Corresponding US-RMAP image of **c**. In **a–d**, the vertical ϕ-axis corresponds to the angular FOV covering 270°, and the horizontal *z*-axis corresponds to the pullback length of 7.2 cm. The approximate mid-dorsal (MD) position and angular measures from the MD are marked along the vertical ϕ-axis. (**e**) Merged volumetric image of **c** and **d**. SP, sphincter; CW, cavity wall. (**f**) A representative *x*-*y* cut near the location indicated by the arrow in **e**. The blue-colored regions represent a lymph node. (**g**) A spectrally-processed PA-RMAP image from the dataset shown in **c**, with the colon signals excluded. This image shows the lymph structures and sO_2 distribution of the surround vasculature outside the colon. The arrows indicate lymph vessels (LV), and the dashed circle corresponds to the left lumbar node (LN) in **h**. CVC, caudal vena cava; CIV, left common iliac vein. (**h**) A post-imaging surgical photo showing the stained lymph node and vessels located outside the colon. This area approximately corresponds to the yellow dashed rectangle in **g**. The horizontal and vertical scale bars in the images represent 1 cm and 5 mm, respectively.